Journal of ELECTRONIC MATERIALS, Vol. 40, No. 6, 2011
DOI: 10.1007/s11664-011-1534-z

Characterizing the Mechanical Properties of Actual SAC105, SAC305, and SAC405 Solder Joints by Digital Image Correlation

T.T. NGUYEN,[1] D. YU,[1] and S.B. PARK[1,2]

1.—Department of Mechanical Engineering, State University of New York at Binghamton, Binghamton, NY 13902, USA. 2.—e-mail: sbpark@binghamton.edu

This paper presents the characterization of the mechanical properties of three lead-free solder alloys 95.5Sn-4.0Ag-0.5Cu (SAC405), 96.5Sn-3.0Ag-0.5Cu (SAC305), and 98.5Sn-1.0Ag-0.5Cu (SAC105) at the solder joint scale. Several actual *ChipArray*® ball grid array (CABGA) packages were cross-sectioned, polished, and used as test vehicles. Compressive tests were performed using a nanocharacterization system over the temperature range of 25°C to 105°C. Images of the cross-sectioned solder joints were recorded by microscope during the tests. The recorded images were then processed by using a digital image correlation (DIC) program to calculate the displacement and strain fields on the solder joints. Finite-element method (FEM) modeling was used to extract the Poisson's ratio, Young's modulus, and coefficient of thermal expansion (CTE) of the solder alloys over the temperature range. The methodology developed in this paper enables characterization of the mechanical properties of the actual solder joints at low strain range with high accuracy.

Key words: Lead-free solder, SAC, solder joint, BGA, mechanical properties, DIC

INTRODUCTION

Solder joint reliability under thermal and mechanical loading is a great concern in electronic packaging. Reliability testing and computational modeling are common methods for reliability assessment. Modeling is more efficient than performing actual reliability tests, which are expensive, time consuming, and require a great deal of manpower for measurement and failure analysis. To support modeling, the material properties of the solder joint are needed. Therefore, it is very important to characterize these material properties accurately to achieve a reliable numerical model.

A number of studies have been reported on the characterization of mechanical properties of lead and lead-free solders. Conventional techniques used for characterization include tensile and compressive tests,[1–5] nanoindentation,[6–8] acoustic wave propagation,[1] and dynamic analyzer.[9] Reviews of mechanical properties of lead-free solders for electronic packaging can be found in Refs. 10 and 11. Most of the above investigations used bulk solder bars as the test vehicles. However, the material properties of the small solder joints used in electronics assembly are different from those of bulk solder bars, because they have significantly different microstructures and different intermetallic compound layers. To account for the effects of microstructures and intermetallic compound distribution, it is necessary to perform characterization on actual solder joints. Among the conventional techniques, nanoindentation can be used for the characterization of mechanical properties of actual solder joints. However, this technique only provides the properties of the individual phases in the solder joints and does not provide a value for the Poisson's ratio. Furthermore, the modulus commonly reported is a measure of the slope between

(Received August 2, 2010; accepted January 19, 2011; published online February 12, 2011)

the origin and a point on the stress–strain curve that may contain some plastic strain.[2] This "secant" modulus is generally an underestimation of the true elastic Young's modulus.

DIC is a full-field optical deformation measurement technique that is widely used to assess in-plane and out-of-plane deformations with subpixel accuracy.[12–17] Moreover, high-resolution electron backscattered diffraction (EBSD), a scanning electron microscopy (SEM)-based technique, has proven to be a potential technique for surface strain mapping applications. It has been increasingly used in recent years to characterize elastic strains and lattice rotations.[18,19] Generally, EBSD provides higher strain measurement resolution than DIC. The spatial resolution can be on the order of several nanometers.[20] EBSD is also the most reliable technique to acquire three-dimensional (3D) crystalline structure and orientation in a solid crystalline phase. However, this technique usually requires specialized sample preparations, where additional chemical polishing of samples is needed after mechanical grinding and polishing. EBSD enables measurement of local deformation over an area that is relatively small compared with that accessible using DIC.[18–20]

In this paper, Poisson's ratio, Young's modulus, and CTE of SAC105, SAC305, and SAC405 were measured on actual solder joints at different temperatures. While the properties of Sn are known to be anisotropic,[21] this work is done to examine how the properties of Sn can be characterized with an isotropic assumption that is desirable for simplifying engineering design. The measurement on actual solder joints was achieved by combining compressive tests, microscope imaging, and DIC processing. Moreover, in this work, backward compressive tests were performed. In these tests, displacements and strains induced by unloading the compressive force were measured. This work has been done assuming that this method minimizes the plastic component of measured displacements and strains so that the elastic component should dominate. A 3D FEM model was built with ANSYS software to simulate the tests. The Poisson's ratio, Young's modulus, and CTE of the solders were extracted by correlating the numerical and experimental results. The methodology developed in this paper enables characterization of the average mechanical properties of the actual solder joints at low strain range with high accuracy, where other conventional methods usually fail.

TEST VEHICLE

The test vehicles are CABGA packages with a 10 × 10 ball grid array (BGA). Three BGA solder alloys of current industrial interest, SAC405, SAC305, and SAC105, were investigated. The solder joint height is 300 μm, while the solder joint diameter is 530 μm. The solder joints were naturally aged at room temperature for several months to bring the microstructure closer to an equilibrium state. The packages were then cross-sectioned into samples containing 3 × 2 solder joints, where each solder joint in the first and the third rows contain only half a solder joint, as shown in Fig. 1. The samples were manually ground and polished using 320 to 1200 grit silicon carbide papers to be ready for the tests. For the solder alloys used in this study the cross-sectioned surfaces of the solder joints were found to have sufficiently detailed contrast features on the surfaces (Fig. 1d) to allow local displacement changes to be measured using DIC calculations. In this paper, it is assumed that the speckle patterns on the cross-sectioned surfaces are consistent with the deformations in the solder joints; the natural speckle patterns on the surfaces were directly used for the DIC measurements, making any further surface treatment unnecessary. The elastic properties of the materials in the mechanical system are shown in Table I.

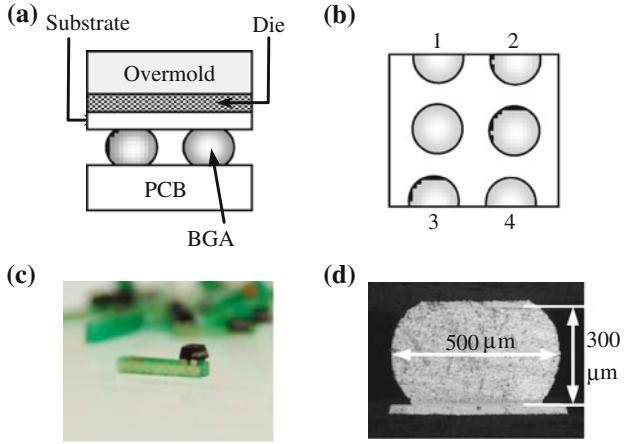

Fig. 1. Test vehicle: (a) front view, (b) top view of the sample, (c) picture of the sample, and (d) polished surface of the solder joint.

Table I. Elastic properties of the constitutive materials

	E (GPa)	CTE (ppm/°C)	*v*
Si	131	2.8	0.28
Cu	129	17	0.34
Substrate	16.8	16	0.3
PCB	26.2	18	0.3
Overmold	20	9	0.3

EXPERIMENTAL PROCEDURES

A schematic of the measurement procedure is shown in Fig. 2. The compressive tests were performed using a customized nanocharacterization system (NCS), which provides an axial displacement resolution of 10 nm and a load cell capacity of 50 N.

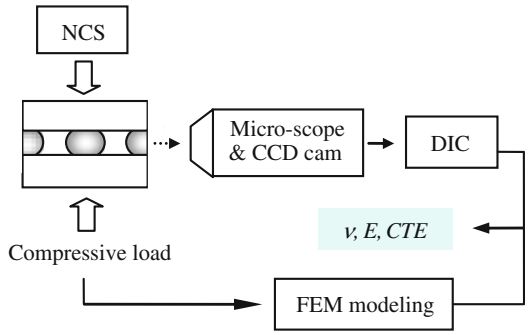

Fig. 2. Schematic of the measurement procedure.

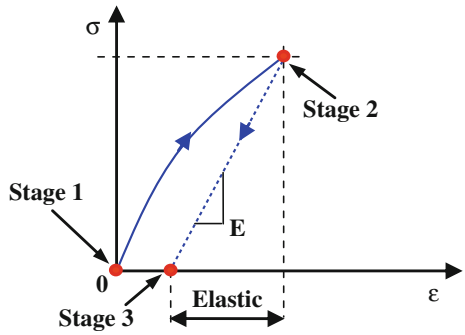

Fig. 3. Microscope imaging sequence.

A charge-coupled device (CCD) camera attached to the top side of a digital microscope was used to image the cross-sectioned surfaces of the solder joints. The images were processed by the DIC-based ARAMIS software to calculate the displacement and strain fields. The material properties were extracted by correlating the DIC and FEM modeling results. In addition, a copper foil heater connected to a power supply was used as the heat source for the tests at high temperatures. A thermal couple was used to monitor the temperature during the tests.

For the in-plane (2D) DIC measurement, magnified 8-bit gray-level images of the cross-sectioned surfaces of the solder joints were projected onto the CCD camera. The sample surface was magnified by using a 20× objective lens, by which a field-of-view size of approximately 522 μm × 697 μm was obtained. As the image resolution is 1292 × 968 pixels, the size of a pixel is roughly 0.5 μm × 0.5 μm. Assuming that the DIC measurement resolution is 0.01 pixels, the measurement resolution of the current setup can be estimated to be 5 nm. This value matches well with the empirical error of the displacement measurement, which was found to be ±0.002 μm in the current setup. This empirical value was obtained by using rigid-body motion technique.[22] In this technique, a reference image of a sample is taken; then a rigid-body motion is generated to the sample; a second image of the sample is taken; finally, the two images are correlated to evaluate local deformations, which are the measurement errors, in the sample. After being mounted into the NCS, the test sample was cured at 100°C for 1 h under a compressive force of 10 N before the tests. This step was found to help produce more uniform displacement and strain fields among the cross-sectioned solder joints. It also improved the cross-sectioned surfaces for the DIC application by providing significant oxidation, thus reducing the glossiness on the surfaces. The sequence of image recording is demonstrated in Fig. 3. Stages 1 and 2 represent the onset and final stage of the compression process, respectively, while stage 3 denotes the stage when the applied compressive force is completely removed. The images of cross-section surfaces taken at stage 2 were correlated with those taken at stage 3 (reference stage) to calculate elastic displacement and strain fields, while images at stage 1 were correlated with those at stage 3 to obtain plastic fields. The displacement and strain fields were obtained for all solder joints from 1 to 4 (Fig. 1b). The final results of each sample are the mean values of the four solder joints. The compressive tests were carried out with the applied forces ranging from 8 N to 32 N at room temperature (25°C), 45°C, 65°C, 85°C, and 105°C. At each temperature at least eight different samples of four cross-sectioned solder joints were used.

For the CTE measurement, the applied force was set to zero. The testing sample was heated from room temperature (25°C) to 105°C. Images of the cross-sectioned surfaces of the solder joints were recorded at every 20°C increase in temperature. The images were correlated with the reference images taken at room temperature to obtain the displacement and strain fields due to thermal expansion.

NUMERICAL MODELING

Since the geometry of the solder joint is not regular, the stress and strain distributions are inhomogeneous inside the solder joint. The stress and strain distributions during the experiment could not be obtained by simple analytical calculations. Therefore, 3D FEM simulation was performed with ANSYS for extraction of the mechanical properties of the solder alloys (Fig. 4). The corresponding forces and temperatures in the experiments were applied to the FEM model. The input parameters of the simulation are the Poisson's ratio (ν), Young's modulus (E), and CTE of the solder alloys. These input parameters were varied until the numerical results matched with the experimental ones.

VALIDATION OF THE MEASUREMENT METHODOLOGY

To validate the developed methodology, we applied it to measure Young's modulus of aluminum. Aluminum was chosen because its Young's modulus is known to be approximately 70 GPa. In addition, the natural surface of aluminum is excellent for DIC measurements.[17] Five aluminum cubic

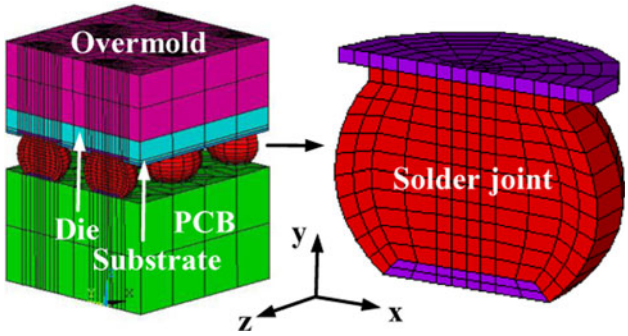

Fig. 4. Three-dimensional FEM model with an enlarged solder joint.

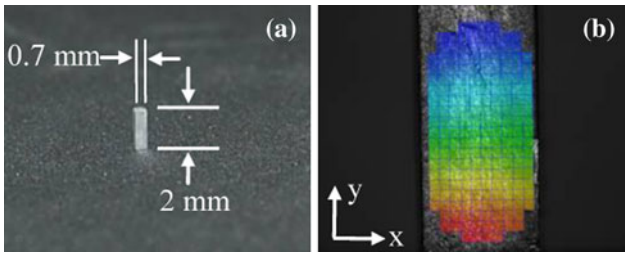

Fig. 5. (a) Aluminum test vehicle and (b) typical contour plot of displacement *Y*.

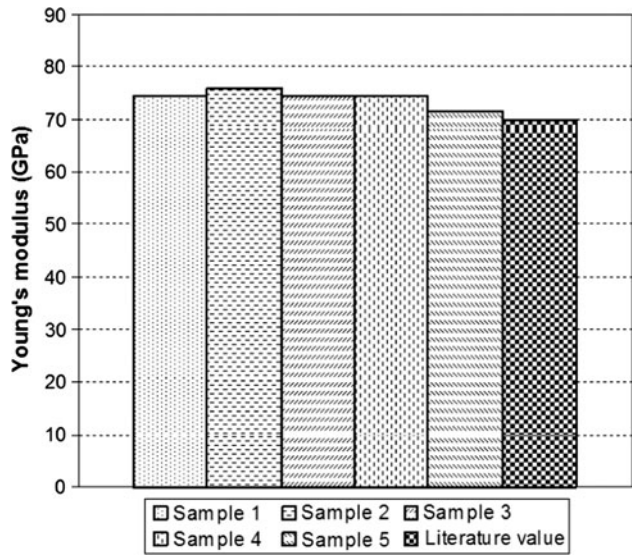

Fig. 6. Young's modulus of aluminum measured using DIC.

blocks with dimensions of 0.7 mm × 0.7 mm × 2 mm were fabricated using a computer numerical control (CNC) machine (Fig. 5a). The blocks were then polished using 1200 grit silicon carbide papers to be ready for the tests. Finally, the above-described measurement procedure was applied to the aluminum samples. Figure 5b shows a typical contour plot of the resultant displacement *Y* due to the compression. The Young's modulus was found to range from 72 GPa to 76 GPa (Fig. 6), in agreement with the literature value. This result validates the measurement methodology.

RESULTS AND DISCUSSION

Typical contour plots of displacement *X* (horizontal direction) and *Y* (vertical direction) fields obtained from the experiments and FEM modeling are shown in Fig. 7. Although the experimental contour plots were not found to be as symmetric as the numerical ones, the numerical and experimental contour plots were found to match relatively well with each other when the values of ν, *E*, and CTE were properly chosen. As such, the compressive behavior of the solder joints was found to be nicely depicted by the contour plots. Locations 1–4 designate areas on the left edge, right edge, top, and bottom of the solder joints, respectively, as shown in Fig. 8. Since the experimentally obtained distributions are not uniform at these locations, displacement *X* was averaged for locations 1 and 2, while displacement *Y* was averaged for locations 3 and 4. Then, the differences between the averaged values of location 1 and 2 and between those of location 3 and 4 are denoted as the total displacements in *X* and *Y* of the solder joint, respectively, in the rest of the paper.

Figure 8a shows the experimental results of the displacement *Y* versus displacement *X* at 25°C. Curve fitting was performed to fit the experimental data. All three solder alloys produce a best fit curve with a slope, which is defined as (displacement *Y*)/(displacement *X*), of approximately 1.44. Since the corresponding slope obtained from FEM is proportional to the input Poisson's ratio of the solder alloys, by simply varying the value of the Poisson's ratio in the FEM model until the modeling produces the same slope we found that $\nu = 0.42$. This value of Poisson's ratio for lead-free solders is, to the best of the authors' knowledge, reported in this paper for the first time. The temperature dependence of this value of Poisson's ratio was found to be negligible over the temperature range.

The relationship between the applied compressive force and displacement *Y* at 25°C is shown in Fig. 8b. Similarly, curve fitting was performed to fit the experimental data. It is noted that almost all of the tests were performed at strain *Y* less than 0.05%. This strain range is hardly achieved by other conventional methods.[10,11] Similarly, the Young's modulus for each solder alloy was extracted by varying its value in the FEM modeling until the modeling produces the same relationship between the force–displacement *Y* as that obtained from the curve fitting.

The resultant values of Young's modulus for the solder alloys are plotted in Fig. 9. The Young's modulus decreases significantly with temperature, as expected. Among the solder alloys, SAC105 has the highest Young's modulus while SAC405 has the lowest one, at 25°C. However, the Young's modulus of SAC105 decreases faster than the others with

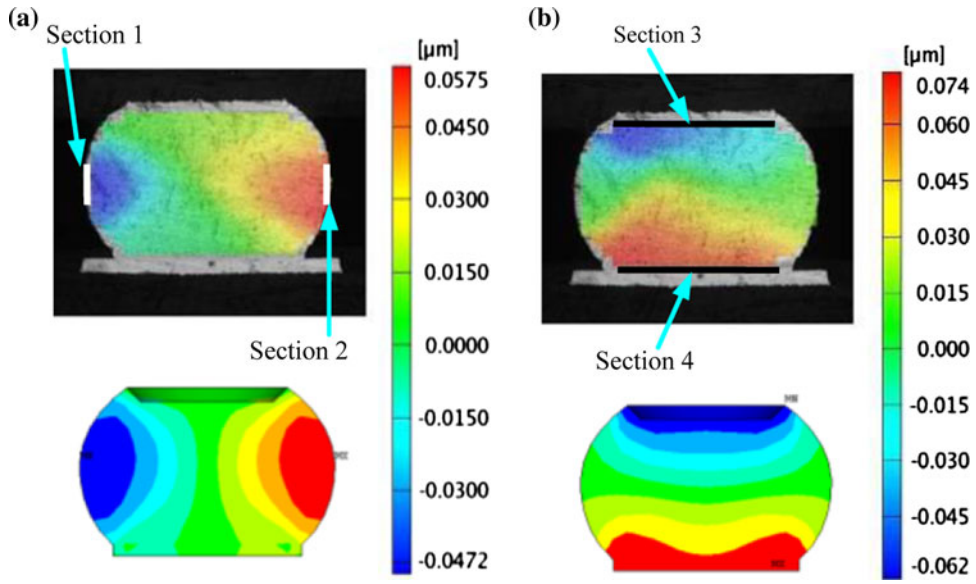

Fig. 7. Typical experimental (top) and numerical (bottom) contour plots of displacement fields (a) *X* and (b) *Y*.

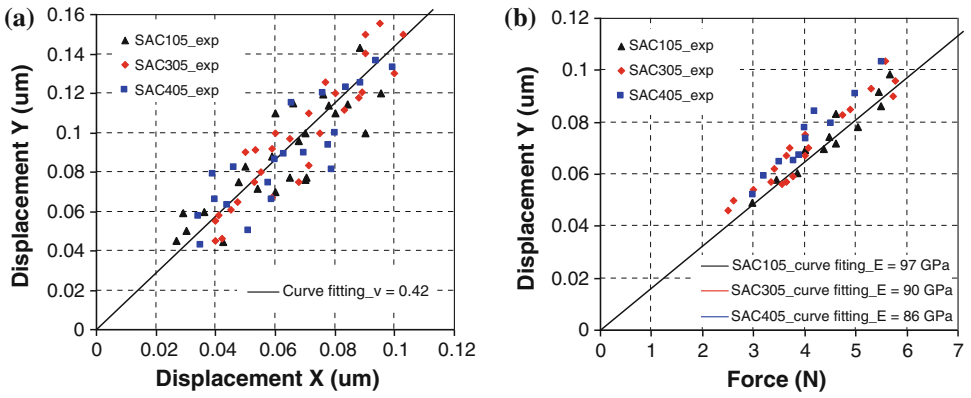

Fig. 8. Experimental data at 25°C: (a) displacement *Y* versus displacement *X* and (b) displacement *Y* versus applied force.

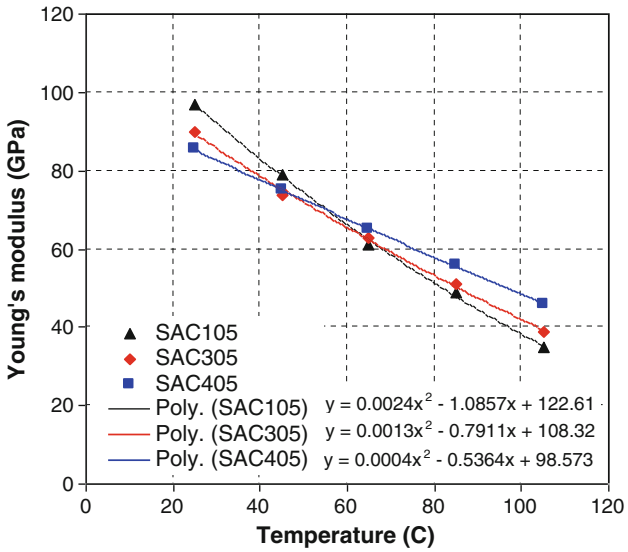

Fig. 9. Temperature-dependent Young's modulus.

temperature and becomes the lowest at 105°C; that of SAC405 becomes the highest at 105°C. Curve-fitting equations of the experimental data are also shown in the figure. The best fit curves exhibit a slightly nonlinear behavior.

The values of Young's modulus found in this paper are higher than literature values, which range from 30 GPa to 66 GPa,[1–11] as expected. This discrepancy is believed to be due to two reasons. Firstly, as mentioned in the "Introduction," extracting elastic modulus from conventional stress–strain curves, which usually contain inelastic strains, could easily lead to an underestimation of the modulus. Secondly, the Young's modulus values reported in this paper are for actual solder joints, where the effect of the intermetallic layers are included, while literature values are for bulk solders, or for single phases in the solder joints (as measured with nanoindentation). It is noted that the values of Young's modulus for intermetallic

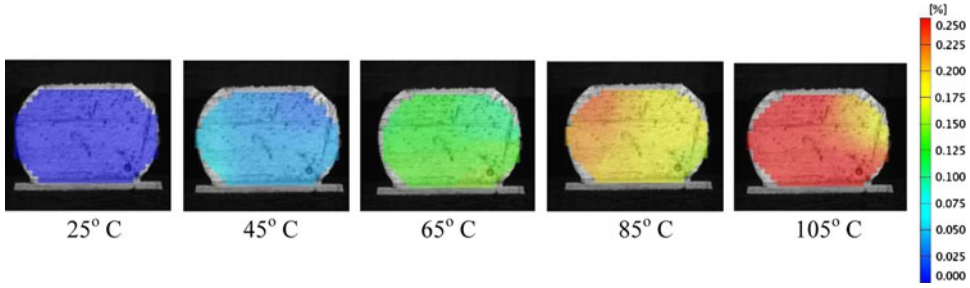

Fig. 10. Contour plots of strain Y due to thermal expansion at 25°C, 45°C, 65°C, 85°C, and 105°C.

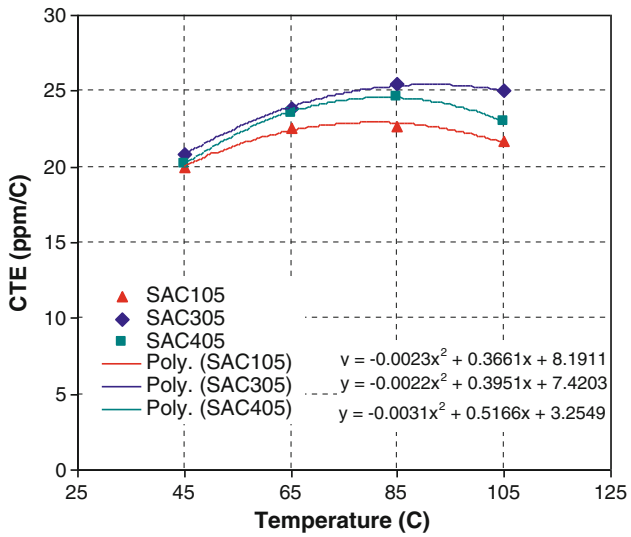

Fig. 11. Secant CTE versus temperature.

compounds within a SAC solder joint, such as Cu_6Sn_5, Cu_3Sn, and Ag_3Sn, which range from 99 GPa to 160 GPa,[23] are much higher than the literature values for SAC solder alloys.

Figure 10 shows typical contour plots of strain Y in the solder joints due to thermal expansion at 25°C, 45°C, 65°C, 85°C, and 105°C. The strain distribution is relatively uniform, as expected. The CTE was extracted by varying its value in the FEM modeling until the displacement Y obtained from the modeling matches with the experimental ones. The resultant secant CTE versus temperature is plotted in Fig. 11. Note that the results are mean values of ten measurements. The results are comparable to literature values for lead-free solder alloys, which range from 16.7 ppm/°C to 26.9 ppm/°C.[10] The behavior of the CTE curves versus temperature is similar to those obtained by Vianco et al.[1] and Deshpande and Sirdeshmukh[24] for SAC405 and tin, respectively. Generally, the CTE values increase with temperature until they reach their convergent values. In this work, the CTE values were found to decrease slightly with temperature after they reached their maximum values. However, this behavior is believed to be due to measurement errors. Curve-fitting equations of the experimental data are also shown in the figure. The best fit curves exhibit strongly nonlinear behavior.

CONCLUSIONS

In this work, a novel methodology was developed for characterization of the mechanical properties of solder joints. Microscope imaging in conjunction with the DIC technique was used to measure the displacement and strain fields in the solder joints during compressive tests, while FEM modeling was used to extract the mechanical properties. The values of Poisson's ratio, Young's modulus, and CTE for three lead-free solder alloys (SAC305, SAC405, and SAC105) were obtained over the temperature range of 25°C to 125°C. The value of Poisson's ratio (ν = 0.42) is reported in this paper for the first time. The values of Young's modulus were found to be higher than literature values for bulk solders, while the values of CTE are in a similar range to literature ones. The Young's modulus and CTE exhibit significant nonlinear temperature dependence. The methodology developed in this paper enables characterization of the mechanical properties of actual solder joints at low strain range with high accuracy. Moreover, it enables the Poisson's ratio to be determined conveniently. Based on the results of this work, future work will focus on characterization of the elastoplastic behavior of solder joints. In addition, anisotropic elastic and CTE of β-Sn grains contained in a SAC solder joint could be explored using this methodology. To reach a smaller scale, SEM and/or transmission electron microscopy (TEM) technique(s) could be used instead of traditional microscopy.

ACKNOWLEDGEMENTS

The authors would like to thank all the members of Opto-Mechanics Lab and Material Lab at Binghamton University for their helpful support.

REFERENCES

1. P.T. Vianco, J.A. Rejent, and A.C. Kilgo, *J. Electron. Mater.* 32, 3 (2003).
2. R.J. McCabe and M.E. Fine, *Scripta Mater.* 39, 2 (1998).
3. R.W. Neu, D.T. Scott, and M.W. Woodmansee, *J. Electron. Packag.* 123, 3 (2001).
4. C. Kanchanomai, Y. Miyashita, and Y. Mutoh, *J. Electron. Mater.* 31, 2 (2002).

5. F. Zhu, Z. Wang, R. Guan, and H. Zhang, *AGEC Proceedings* (2008), pp. 107–112.
6. F. Gao, H. Nishikawa, T. Takemoto, and J. Qu, *Microelectron. Reliab.* 49, 3 (2009).
7. S.Y. Chang, Y.C. Huang, and Y.M. Lin, *J. Alloy Compd.* 490, 1 (2010).
8. M. Erinc (Ph.D. dissertation, Eindhoven University of Technology, 2007).
9. M.R. Harrison, J.H. Vincent, and H.A.H. Steen, *Solder. Surf. Mt. Technol.* 13, 3 (2001).
10. H. Ma and J.C. Suhling, *J. Mater. Sci.* 44, 5 (2009).
11. http://www.metallurgy.nist.gov/solder/clech/Sn-Ag-Cu_Main.htm. Accessed 16 April 2010.
12. H.A. Bruck, S.R. McNeill, M.A. Sutton, W.H. Peters III, *Exp. Mech.* 29, 261 (1989).
13. B. Pan, K. Qian, H. Xie, and A. Asundi, *Meas. Sci. Technol.* 20, 6 (2009).
14. J.B. Kwak, D.G. Lee, T.T. Nguyen, and S.B. Park, *IMECE Proceedings* (2009), pp. 1–8.
15. T.T. Nguyen, D.G. Lee, J.B. Kwak, and S.B. Park, *Microelectron. Reliab.* 50, 7 (2010).
16. Y. Sun and J.H.L. Pang, *Microelectron. Reliab.* 48, 2 (2008).
17. F.M. Sánchez-Arévalo and G. Pulos, *Mater. Charact.* 59, 11 (2008).
18. A.J. Wilkinson, E.E. Clarke, T.B. Britton, P. Littlewood, and P.S. Karamched, *J. Strain Anal. Eng.* 45, 5 (2010).
19. A.J. Wilkinson and D. Randmany, *Philos. Mag.* 90, 9 (2010).
20. S. Villert, C. Maurice, C. Wyon, and R. Fortunier, *J. Microsc.* 233, 2 (2009).
21. S. Park, R. Dhakal, L. Lehman, and E. Cotts, *Acta Mater.* 55, 9 (2007).
22. H. Haddadi and S. Belhabib, *Opt. Laser Eng.* 46, 2 (2008).
23. R.R. Chromik, R.P. Vinci, S.L. Allen, and M.R. Notis, *JOM* 55, 6 (2003).
24. V.T. Deshpande and D.B. Sirdeshmukh, *Acta Cryst.* 15, 3 (1962).